Available online at www.sciencedirect.com

jmr&t Journal of Materials Research and Technology

journal homepage: www.elsevier.com/locate/jmrt

Original Article

Nanofabrication of $(Cr_2O_3)_x$ $(NiO)_{1-x}$ and the impact of precursor concentrations on nanoparticles conduct

Naif Mohammed Al-Hada [a,*], *Abbas M. Al-Ghaili* [b,**], *Hairoladenan Kasim* [c,***], *Muneer Aziz Saleh* [d], *Hussein Baqiah* [a], *Jian Liu* [a], *Jihua Wang* [a,****]

[a] *Shandong Key Laboratory of Biophysics, Institute of Biophysics, Dezhou University, Dezhou, 253023, China*
[b] *Institute of Informatics and Computing in Energy (IICE), Universiti Tenaga Nasional (UNITEN), 43000, Kajang, Selangor, Malaysia*
[c] *College of Computing & Informatics (CCI), Universiti Tenaga Nasional (UNITEN), 43000, Kajang, Selangor, Malaysia*
[d] *School of Chemical and Energy Engineering, Universiti Teknologi Malaysia, 81310, Skudai, Johore Bahru, Johore, Malaysia*

ARTICLE INFO

Article history:
Received 27 September 2020
Accepted 3 January 2021
Available online 6 January 2021

Keywords:
$(Cr_2O_3)_x$ $(NiO)_{1-x}$ nanoparticles
Calcination technique
Structural properties
Optical properties

ABSTRACT

This study aims to synthesize the $(Cr_2O_3)_x$ $(NiO)_{1-x}$ nanoparticles at lower and higher precursor values using the calcination method. There is a lack in regard to investigating the lower and higher precursor values on structural and optical properties of the $(Cr_2O_3)_x$ $(NiO)_{1-x}$ nanoparticles. To synthesize the $(Cr_2O_3)_x$ $(NiO)_{1-x}$ nanoparticles, Cr (III) acetate hydrate and Ni (II) acetate tetrahydrate were reacted with poly (vinyl alcohol). Several techniques, including X-ray diffraction (XRD), transmission electron microscopy (TEM) and Fourier transform infrared spectroscopy (FT-IR), have been employed to characterize the synthesized sample. The XRD pattern analysis indicated that, following calcination, nanoparticle formation occurred, indicating hexagonal crystalline structures (HCP) and face-centred cubic (FCC) of $(Cr_2O_3)_x$ $(NiO)_{1-x}$ nanoparticles. FT-IR verified the existence of Ni−O and Cr−O as the original compounds of ready $(Cr_2O_3)_x$ $(NiO)_{1-x}$ nanoparticle samples. In term of average particle size, this varied from 5 to 16 nm when the precursor concentration rised from $x = 0.20$ to $x = 0.80$, as reflected in the TEM results. X-ray photoelectron spectroscopy (XPS) was employed to measure the valence state and surface composition of the prepared product nanoparticles. To identify the optical band gap using the Kubelka−Munk equation, diffuse UV−visible reflectance spectra were employed, which revealed that the energy band gap fell with a rise in the value of x. In addition, photoluminescence (PL) spectra indicated that the photoluminescence intensity was related to a directly

* Corresponding author.
** Corresponding author.
*** Corresponding author.
**** Corresponding author.
E-mail addresses: naifalhada@yahoo.com (N.M. Al-Hada), abbasghaili@yahoo.com (A.M. Al-Ghaili), hairol@uniten.edu.my (H. Kasim), jhw25336@126.com (J. Wang).
https://doi.org/10.1016/j.jmrt.2021.01.007

proportional way to particle size. Hence, the results can be employed with a broad range of applications in solar cell energy applications at higher x values and antibacterial activity at lower x values.

1. Introduction

Research activity in the field of nanomaterials has been growing significantly in recent years, and some researchers have been interested in leveraging the distinctive physico-chemical properties of nanomaterials [1–9]. These research initiatives have led to novel systems, nanoplatforms, devices, and structures that can be applied in numerous areas [6,10–20]. An advantage of biodegradable, biocompatible, and functionalized nanomaterial applications relates to the fact that an increasing number of publications have focused on this area [21–30]. An increasingly prominent issue involves the use of nickel oxide with face-centred cubic (FCC) and chromium oxide with hexagonal close-packed (HCP) structures, in semiconductor nanomaterials, which has been investigated more and more in empirical studies [31–35]. Given its II-IV composite semiconductor status, NiO contains both group II and group IV elements (i.e., in terms of the periodic table) [36]. Many applications have sought to leverage the unique structural characteristics of the nanomaterial-based on desirable chemical and physical properties [37–39]. NiO has a notable FCC crystalline structure, along with a n-type indirect and direct energy band gaps amounting to 3.5–3.8 eV [39–41]. Multiple physical applications of NiO have been reported, including NiO semiconductors nanostructures [42–44]. In these devices, the high internal viability of visible light waves means that they are valuable in photovoltaic applications (e.g., solar cells) [45,46]. Additionally, diodes, transparent electrodes, and gas sensors are other notable applications, and antibacterial properties are also worth considering [47]. A range of NiO nanostructures can serve varying purposes depending on the nanoscale [48]. Examples include nanoparticles [49], nanocrystals [44], nanoclusters [50], nanowires [51,52], nanotubes [53], nanoflowers [54], and NiO nanoflake arrays [55].

In a similar way, hexagonal chromium (III) oxide (Cr_2O_3) is classified as a composite semiconductor, II-VI, which consists of the metal Cr (II) and the non-metallic element oxygen (VI) [41]. A range of Cr_2O_3 semiconductor materials have been associated with noteworthy properties, as a result of which valuable applications have been developed [56,57]. This structure is employed as the standard hexagonal crystal structure, and in terms of its classification, it is viewed as a p-type semiconductor with 3.00 and 3.40 eV with direct band gaps [29,40]. Therefore, given the distinctive properties of Cr_2O_3 nanomaterials, which derive from their unique crystal structure and the dimensions of the nano-sized particle, a range of studies and applications have leveraged these features. Examples include use as solar cells [58], and optoelectronic devices [59], as well as the focus on exploiting the pellucidity that exists in the observable area of the solar spectrum. Additional applications include catalysis [60], diodes [61], gas sensors [62], and biomedical tools [57]. Multiple methods have been used to generate diverse types of Cr_2O_3 nanomaterial, including nanocrystals [63], nanoclusters [64,65], nanotubes [66], and nanorods [67]. As the literature suggests, a range of techniques can be used to fabricate Cr_2O_3 nanomaterials, including sonochemical [68], solvothermal [69], co-precipitation [70], microwave hydrothermal [71], thermal [72], and sol–gel treatment [34].

Nevertheless, the distinctive composition of $(Cr_2O_3)_x$ $(NiO)_{1-x}$, in terms of the band gaps and sizes that grow from both oxide semiconductors, reflects the complementary features. There is also the potential likelihood of displaying unique features compared to different singular semiconductor components. A critical issue to consider that relates to the distinctive composition of $(Cr_2O_3)_x$ $(NiO)_{1-x}$ nanocomposites relates to the utilization of $(Cr_2O_3)_x$ $(NiO)_{1-x}$ with biocides, disinfectants, and other purposes. Compared to organic-based materials, the composition is significantly more stable and has a longer life, and it is also researched more intensely in the field of biological activity [73,74] $(Cr_2O_3)_x$ $(NiO)_{1-x}$ nanostructures can be generated in various ways, including thermal decomposition, the co-precipitation method [75], and the chemical method [76]. However, the production of $(Cr_2O_3)_x$ $(NiO)_{1-x}$ nanoparticles on an industrial scale using these methods is limited owing to the complex nature of the synthesis process. In particular, it requires long reaction times, toxic reagents, and effluent by-products. Furthermore, these methods do not generate the product in powder form. There are also no studies on the heat treatment synthesis of $(Cr_2O_3)_x$ $(NiO)_{1-x}$ nanoparticle at different x values. Hence, to address the limitations mentioned above, this study examines the heat treatment technique in producing pure powder oxide nanoparticles. To produce no waste $(Cr_2O_3)_x$ $(NiO)_{1-x}$ nanoparticles products, a straightforward heat treatment route is used. This research is novel since it seeks to generate the product in a way that is worthwhile for industrial applications, focusing on simple handling, particle in different size. Indeed, smaller size can be used in antibacterial activity, and bigger size can be used in energy application [77]. Other advantages are low cost, high-quality, high adaptability, in powdered form, and with an effective band gap. Notably, the present technique does not necessarily requires additional chemical reagents. This paper focuses on a novel technique and the impact of precursor values for producing a $(Cr_2O_3)_x$ $(NiO)_{1-x}$ nanosize. The obtained results have revealed that the smaller particle size is obtained from lower x values and the smaller energy band gap is obtained from higher x values. From these results, it is suggested that the

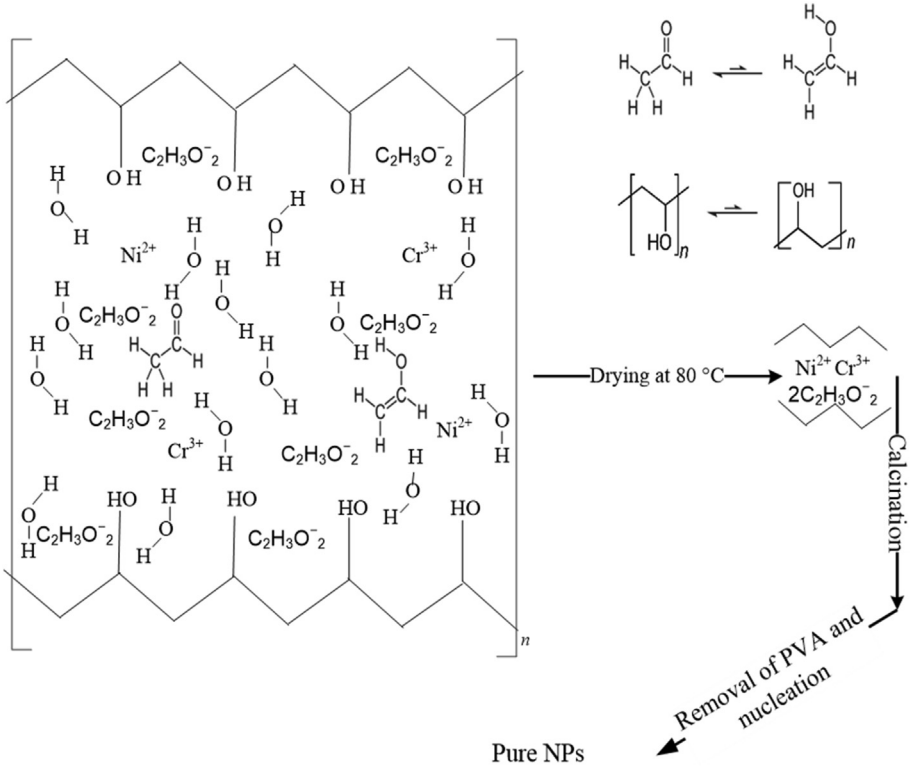

Fig. 1 – A proposed mechanism of the $(Cr_2O_3)_x$ $(NiO)_{1-x}$ nanoparticles growth.

product at lower x values and higher x values can be used with antibacterial activity and solar cell energy applications, respectively.

The technique given in this paper uses a thermal-based treatment process for the synthesis of $(Cr_2O_3)_x$ $(NiO)_{1-x}$ samples. In addition, it investigates the impact of Cr_2O_3 and NiO contents on the structural, morphological, and optical features of $(Cr_2O_3)_x$ $(NiO)_{1-x}$ nanoparticle. The technique relies on a solution containing metal acetate ions as predecessors and a poly (vinyl alcohol), which serves as a capping agent. However, a required calcination technique was undertaken for the purpose of producing pure desirable nanoparticles. The product's morphology and crystallinity have been examined using a range of techniques, and the study also focused on the variable of x values.

2. Experimental work

2.1. Materials

The following metal precursors were used in this experiment: (0.20, 0.40, 0.60, 0.80 and 1.00 mmol) of Cr (III) acetate and (0.20, 0.40, 0.60, 0.80 and 1.00 mmol) of the Ni (II) acetate. Additionally, the capping agent was polyvinyl alcohol (PVA), which facilitated particle dispersal, and deionized water was used as a solvent. Synthesis of $Cr_2(CH_3CO_2)_4 \bullet 2(H_2O)$ (99%), $Ni(OCOCH_3)_2 \bullet 4H_2O$ (99%), and PVA (MW = 61,000) took place using Sigma–Aldrich. The chemicals used throughout this study's experiments were procured from Sigma–Aldrich in the United States, and they were research-grade in terms of quality. All chemicals were used without additional purification.

2.2. Samples preparation

At the outset, 4 g of poly (vinyl alcohol)was dissolved in 100 ml of deionized water to prepare the $(Cr_2O_3)_x$ $(NiO)_{1-x}$ nanoparticle product. In turn, vigorous stirring occurred for 2 h at 70 °C. Following this, Cr (III) acetate hydrate $Cr_2(CH_3CO_2)_4 \bullet 2(H_2O)$ was dissolved in the following quantities: 0.00, 0.20, 0.40, 0.60, 0.80, and 1.00 mmol. Afterward, to facilitate the formation of a homogenous solution, Ni (II) acetate tetrahydrate $Ni(OCOCH_3)_2 \bullet 4H_2O$ was combined and vigorously mixed in the following quantities: 1.00, 0.80, 0.60, 0.40, 0.20, and 0.00 mmol. The combined solution was then moved inside a Petri dish, after which an oven was used to dry it for 24 h at 80 °C. The solid that resulted from this process was crushed for 30 min in a mortar, thereby attaining a powdered form. A calcination temperature of 700 °C was then applied to the powder, using a box furnace, and this lasted 90 min. This completed the as-synthesized and calcined oxide nanoparticle samples, meaning they were ready for characterization.

2.3. Characterization

Several techniques were employed to study the structural, morphological, and optical features of the samples. X-ray diffraction was employed to record observed measurements, using Cu Kα (λ = 1.54187 Å) radiation at 40 kV and 30 mA. Using the range of 280–4000 cm^{-1}, Fourier transform infrared (FTIR)

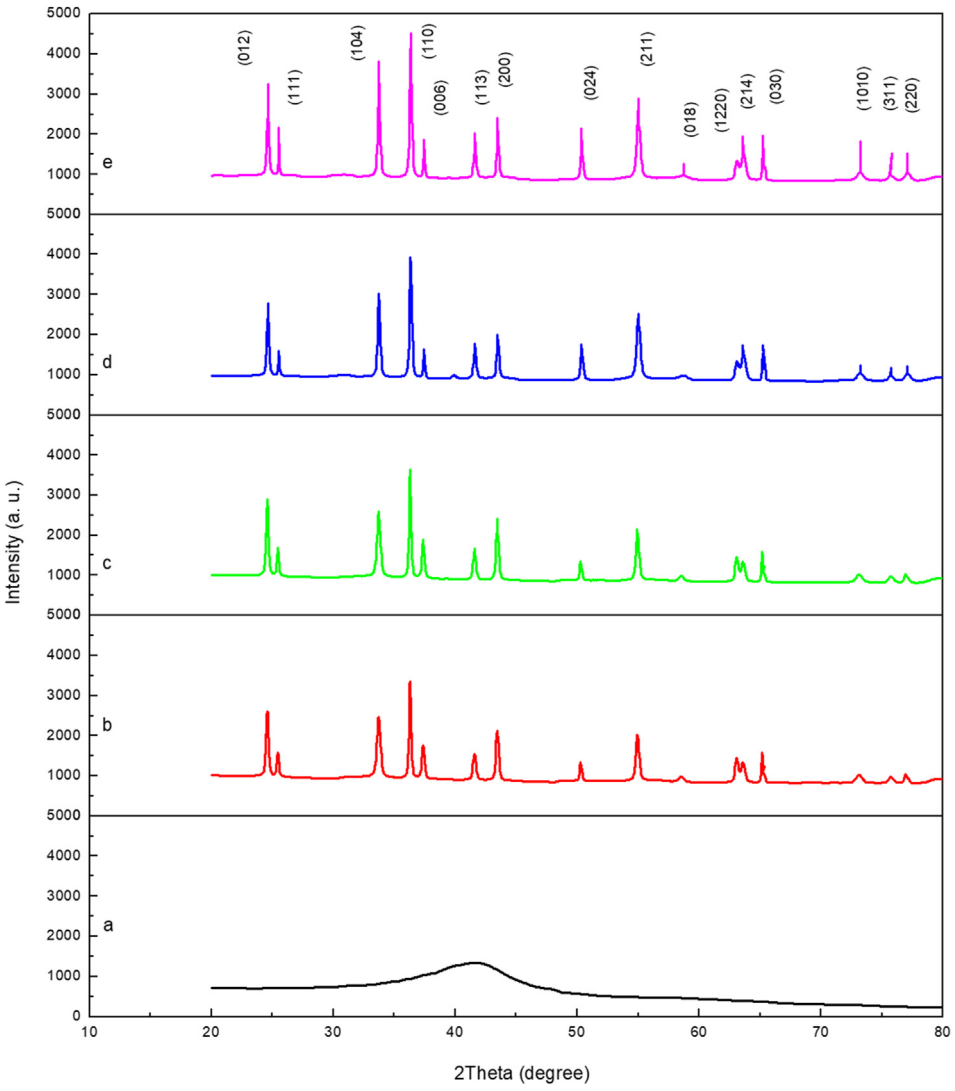

Fig. 2 – XRD patterns of (a) no calcination, (b) $(Cr_2O_3)_{0.20}$ $(NiO)_{0.80}$, (c) $(Cr_2O_3)_{0.40}$ $(NiO)_{0.60}$, (d) $(Cr_2O_3)_{0.60}$ $(NiO)_{0.40}$ and (e) $(Cr_2O_3)_{0.80}$ $(NiO)_{0.200}$.

spectroscopy measurements have been taken. Additionally, transmission electron microscopy (TEM) images were acquired. The wide scan analysis was undertaken using the X-ray photoelectron spectroscopy (XPS) with a pass energy amounting to 280 eV (with 1 eV for each step). To assess the sample optical properties in the 200–800 nm range in terms of wavelength, a ultraviolet–visible (UV–vis) spectrophotometer was employed. Furthermore, photoluminescence (PL) was measured based on a PerkinElmer spectrofluorometer LS-55, which was equipped with a xenon lamp. This measurement took place at room temperature (RT). All investigations have been done at RT.

3. Results and discussion

3.1. *Formation of mechanism of nanoparticles*

Fig. 1 provides an overview of the mechanism and behavior of the nanoparticles in the course of calcination. The main aim of poly (vinyl alcohol) was to stabilize the complex metallic salts produced [78]. On many occasions, this is achieved using side steric and electrostatic stabilization for the amide groups linked to poly (vinyl alcohol) chains and linked to the methylene groups. When blending the solution continues, the suppression of metallic ions occurs, and amine groups again capture them by ionic dipole created inside polymeric chains. In turn, in the drying phase, the metallic cations stop moving inside the cavity polymer chain. This is attributable to H_2O loss. When the next calcination stage occurs, various gases evolve as the decomposition of organic materials occurs. These gases include N_2, NO, CO, or CO_2. Additionally, in the calcination stage, metal oxide nanoparticle nuclei production is influenced by poly (vinyl alcohol). Thus, in the absence of poly (vinyl alcohol), the Ostwald ripening process would advance, which leads to an increase in nanoparticle size with higher surface energy levels. Nevertheless, poly (vinyl alcohol) presence deactivates steric hindrance that affects nanoparticle conglomeration. Hence, poly (vinyl alcohol) amendment can stimulate a reduction in nanoparticle grain size,

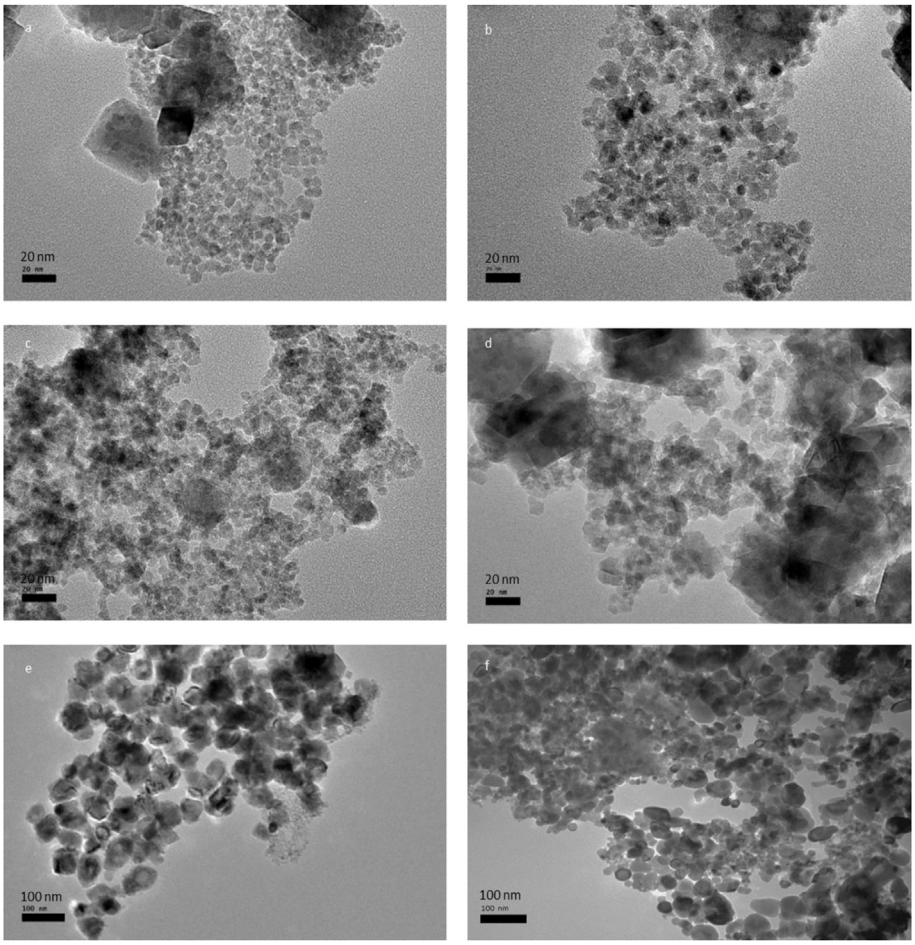

Fig. 3 – TEM images of (a) $(Cr_2O_3)_{0.20}$ $(NiO)_{0.80}$, (b) $(Cr_2O_3)_{0.40}$ $(NiO)_{0.60}$, (c) $(Cr_2O_3)_{0.60}$ $(NiO)_{0.40}$, (d) $(Cr_2O_3)_{0.80}$ $(NiO)_{0.200}$, (e) $(Cr_2O_3)_{1.00}$ $(NiO)_{0.00}$ and (f) $(Cr_2O_3)_{0.00}$ $(NiO)_{1.00}$ nanoparticles calcined at 700 °C.

which stems from the restriction of metal ion breakdown on nanoparticle surfaces [79–85].

3.2. *XRD analysis*

Fig. 2 provides an overview of the XRD pattern $(Cr_2O_3)_x$ $(NiO)_{1-x}$ nanoparticles following the calcination process, which took place at 700 °C for 3 h. As shown in Fig. 2 (b-e), the triangle and square mark the diffraction peaks for the NiO and Cr_2O_3 nanoparticles. A broad spectrum was exhibited at the sample before calcination treatment, which suggested that the sample is still in an amorphous stage, as shown n Fig. 2a. In the XRD pattern, the diffraction peaks are typical values corresponding to NiO (FCC) and Cr_2O_3 (HCP) nanoparticles. Consistent with the JCPDS Card 36–1451 [29,86], the NiO nanoparticles' peaks are matched effectively to (111), (200), (220), and (311) planes. In a similar way, as indicated by the JCPDS Card 38–1479 [72,87], the peaks of Cr_2O_3 are matched to (012), (104), (110), (006), (113), (024), (211), (018), (214), (030), (211), (010), and (220) planes. The synthesised $(Cr_2O_3)_x$ $(NiO)_{1-x}$ nanoparticles displayed a combination of the cubic phase of NiO nanoparticles and hexagonal Cr_2O_3 nanoparticles. Notably, in terms of peaks, no other contamination peak has been identified in the samples' XRD patterns. The crystal size, which is denoted *D*, for the nanoparticles can be calculated from the most intense peak (110) using the formula given below, known as Scherrer's formula [77,88]:

$$D = (0.9\lambda)/(\beta\cos\theta)$$

where λ is the X-ray wavelength (1.5406 Å), β is the full width at half maximum, and θ is the angle of diffraction. Therefore, the crystallite size rose from 5 to 15 nm when the values of x rose to 1.00 mmol Chromium acetate. Hence, the findings indicate that an increase in the x value leads to a sharper and narrower diffraction peak, accompanied by higher intensity. This is shown in Fig. 2 (c, d, f). The higher particle size in the case of the nuclei promotes the results regarding crystalline volume ratio, causing them to increment and contribute to the reinforcement and enhancement of crystallinity [89,90].

3.3. *TEM analysis*

Sample nanoparticle characterization relied on TEM evaluation. It is usually the case for samples to show homogeneous morphological features, as shown in Fig. 3 (a–f). The figure shows TEM images, in this case $(Cr_2O_3)_x$ $(NiO)_{1-x}$ nanoparticles, which were calcined at 700 °C. An important feature

of TEM analysis is that it verifies the uniform spherical shape of the nanoparticles produced. As previously noted, x values are directly and proportionally related to particle size, where particle size rises ascribable to the accumulation of contiguous particles (which itself occurs from the surface melting at greater calcination temperatures and x values).

The results indicated that the $(Cr_2O_3)_x$ $(NiO)_{1-x}$ nanoparticles have been homogeneous and in spherical shape. Furthermore, the results demonstrated that they were not an issue to crystal tangle, as revealed by TEM images focusing on the synthesized $(Cr_2O_3)_x$ $(NiO)_{1-x}$ nanoparticles. The typical process showed how efficient it could be in producing sample nanoparticles, where a noticeable PVA existence affects nanoparticle size through the agglomeration–suppression mechanism. Table 1 provides an evaluation of the XRD and TEM results. In particular, it shows a relationship between particle sizes of 5 and 16 nm and heating treatment at 700 °C. PVA operates as a stabilizer for particles, and it facilitates nucleation and development of the nanoparticle. It has also been shown to promote consistency. Hence, it can be used to limit the size of nanoparticles, and also to safeguard against the agglomeration of nanoparticles [17,85,91–94].

Based on the broad sample band observed in the XRD patterns, the reasonable assumption was made that NiO nanoparticles are significantly smaller compared to Cr_2O_3-nanoparticles. Hence, the use of Cr_2O_3concentration in the sample (x = 0.20 to x = 0.80) led to a rise in particle size, which can be ascribed to the greater aggregation level. Regarding the decreasing trend, one way to account for this may stem from differences in the ionic crystal radii of Cr^{3+} and Ni^{2+}. Given that the ionic radius of Cr^{3+} is larger in relation to Ni^{2+}, it is worth noting that a substitutional defect usually occurs. This happens when the NiO atom replaces its Cr_2O_3 counterpart in the crystal lattice site of Cr_2O_3solid. In turn, this leads to lattice stress, which leads to a disturbance in particle growth.

3.4. *FT-IR analysis*

Fig. 4 (a) shows all absorption bands which are ascribed to the PVA and metal oxide nanoparticles. The sample at RT, 3414, 2945, and 1646 cm^{-1} wave number have been allocated to N–H, C–H, and C = O stretching vibrations, respectively.

Table 1 – XRD and TEM results for $(Cr_2O_3)_x$ $(NiO)_{1-x}$ nanoparticles at various x.

Sample	Crystallite size (XRD) (nm)	Particle size (TEM) (nm)
$(Cr_2O_3)_{0.20}$ $(NiO)_{0.80}$	5 ± 0.50	5 ± 2
$(Cr_2O_3)_{0.40}$ $(NiO)_{0.60}$	7 ± 0.70	8 ± 3
$(Cr_2O_3)_{0.60}$ $(NiO)_{0.40}$	8 ± 0.40	9 ± 2
$(Cr_2O_3)_{0.80}$ $(NiO)_{0.20}$	15 ± 0.50	16 ± 4
$(Cr_2O_3)_{1.00}$ $(NiO)_{0.00}$	39 ± 0.30	40 ± 3
$(Cr_2O_3)_{0.00}$ $(NiO)_{1.00}$	20 ± 0.40	22 ± 2

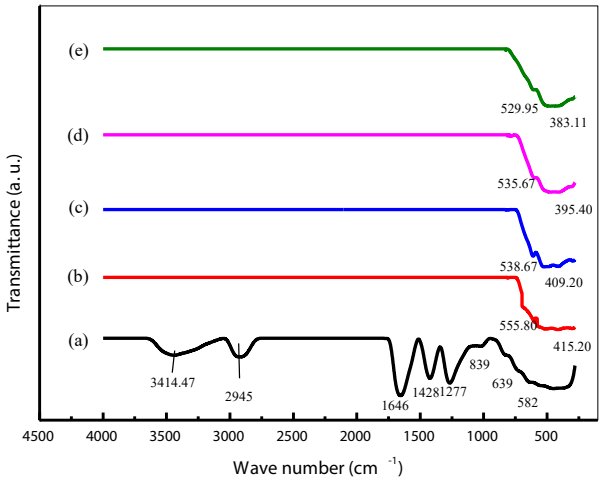

Fig. 4 – FTIR spectra of (a) no calcination, (b) $(Cr_2O_3)_{0.20}$ $(NiO)_{0.80}$, (c) $(Cr_2O_3)_{0.40}$ $(NiO)_{0.60}$, (d) $(Cr_2O_3)_{0.60}$ $(NiO)_{0.40}$, and (e) $(Cr_2O_3)_{0.80}$ $(NiO)_{0.200}$ nanoparticles calcined at 700 °C.

Additional, the sample at 1428 cm^{-1} wave number has been attributed to C–H bending vibration originated, whereas 1277 cm^{-1} was related to C–N stretching vibration. Lastly, 839, 639, and 582 cm^{-1} have been matching to the vibrations occurred outstanding to C–C ring and C–N = O bending [18,40,83,95,96]. Fig. 4 (b-e) provides an overview of the FT-IR spectrum, which was attained at 280–4000 cm^{-1} for the sample nanoparticles formed by the calcination technique summarized above. The dual absorption bands were attributed to the production of outstandingly pure sample nanoparticles, which was also reflected by a movement in the wave number for the $(Cr_2O_3)_x$ $(NiO)_{1-x}$ nanoparticles spectra accompanying with rising x values. In the case of the x effect, evidence for this was also suggested by the crystallinity improvement associated with the resulting $(Cr_2O_3)_x$ $(NiO)_{1-x}$ nanoparticles. Hence, Fig. 4 indicates that the x-related increment leads to a characteristically more pointed peak for the sample, demonstrating that an increasing x value is linked to more prominent crystalline natures for the resulting metal oxide. Each of the characteristic infrared bands associated with the samples, that is, with x = 0.20 to x = 0.80, was identified inside the Cr–O, and Ni–O stretching vibrations range. This can be considered as adequate proof of the fact that the samples are pure $(Cr_2O_3)_x$ $(NiO)_{1-x}$ nanoparticles. As such, the samples do not have further impurities.

3.5. *XPS analysis*

To identify the chemical state and phase compositions of Ni, Cr, and O, X-ray photoelectron spectroscopy (XPS) analysis has been successfully used. Fig. 5a provides the high-resolution XPS spectra for the existence of the O 1s element. Furthermore, Fig. 5b–c illustrates the XPS spectra for Cr 2p and Ni 2p, respectively. In the case of the XPS spectrum for Cr, this is concerned with corresponding binding energies of 578 eV and 585 eV for Cr $2p_{3/2}$ and Cr $2p_{1/2}$ peaks (see Fig. 5b) [72]. It is worth emphasizing that comparable results have been reported elsewhere in the literature. In Fig. 5c, Ni $2p_{3/2}$

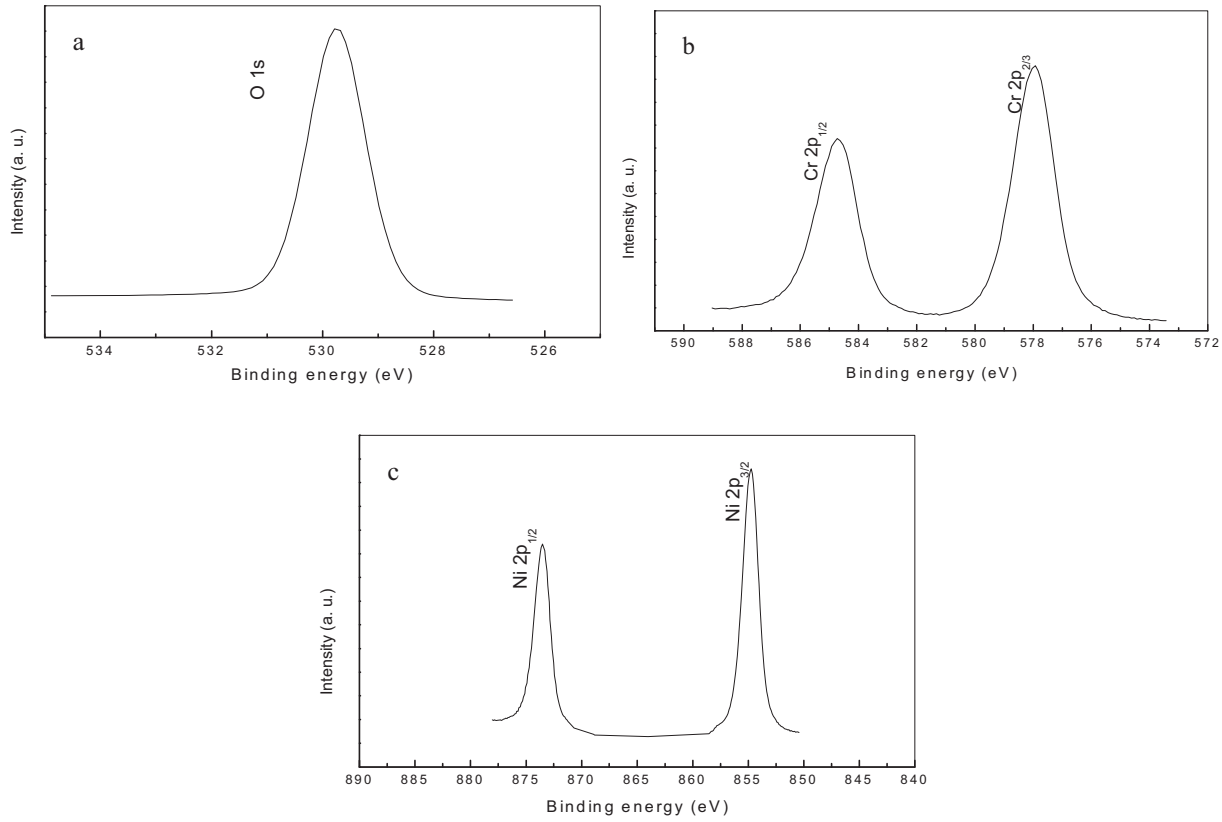

Fig. 5 – The XPS spectra of nanoparticles (a) Oxygen, (b) Cr and (c) Ni.

and Ni 2p1/2 have a binding energy of 855 eV and 875.5 eV, corroborating nickel's 2+ oxidation state [97]. In the case of Fig. 5a, this shows the O 1s spectrum, indicating the existence of two oxygen types with binding energies at 531.2 eV [77]. It is important to recognize that, in the case of the former, this correlates with Cr_2O_3, while in the case of the latter, this correlates with NiO. Furthermore, the results show that every element in the nanoparticle has pure oxidation states in the absence of all impurities.

3.6. *Band gap study*

The Kubelka–Munk function involves plotting the Kubelka–Munk function's square, that is, $(F(R_\infty)h\nu)^2$ against energy, and then extending the curve's linear portion to $F(R)^2 = 0$ [98–101]. The function is used to calculate direct energy band gaps for nanoparticles based on diffuse reflectance spectra for samples heated at a temperature of 700 °C, as represented in Fig. 6a-d. This shows that, for the oxide nanoparticles, the bandgap energy has been produced. An inversely proportional relationship has been identified between energy band gap values and the x value. When the x value increases, this is generally attributed to quantum size effects. Moreover, the reduction that takes place with respect to the bandgap can be ascribed to the transitions between the partly appropriate valence and the conduction bands for the d-shell electrons of Cr^{3+} ions [102–104].

With the abovementioned considerations in mind, excluding the particle size impact in terms of the bandgap is complex. Due to the reduction of particle size, a change can be achieved in the material properties and band structure. However, the size of nanoparticles increases in line with a

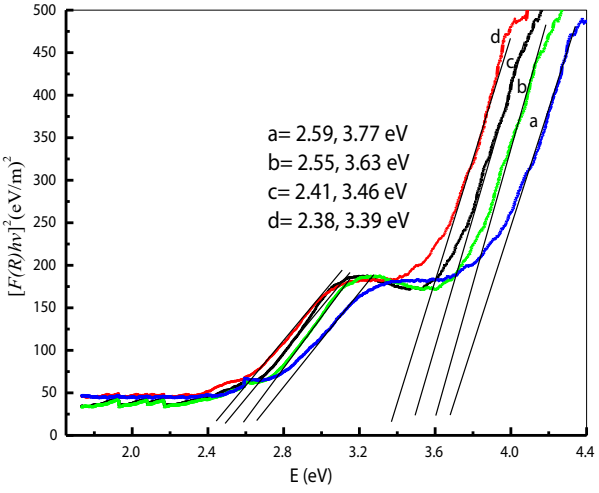

Fig. 6 – The energy band gap of (a) $(Cr_2O_3)_{0.20}$ $(NiO)_{0.80}$, (b) $(Cr_2O_3)_{0.40}$ $(NiO)_{0.60}$, (c) $(Cr_2O_3)_{0.60}$ $(NiO)_{0.40}$, and (d) $(Cr_2O_3)_{0.80}$ $(NiO)_{0.20}$ nanoparticles at calcination temperature of 700 °C.

Table 2 – Energy band gap of nanoparticles at different concentrations of x.

x values	x = 0.20	x = 0.40	x = 0.60	x = 0.80
$(Cr_2O_3)_x$ $(NiO)_{1-x}$ Nanoparticles	Eg (eV)			
Cr_2O_3	2.59 ± 0.04	2.55 ± 0.06	2.41 ± 0.09	2.38 ± 0.07
NiO	3.77 ± 0.05	3.63 ± 0.02	3.46 ± 0.07	3.39 ± 0.04

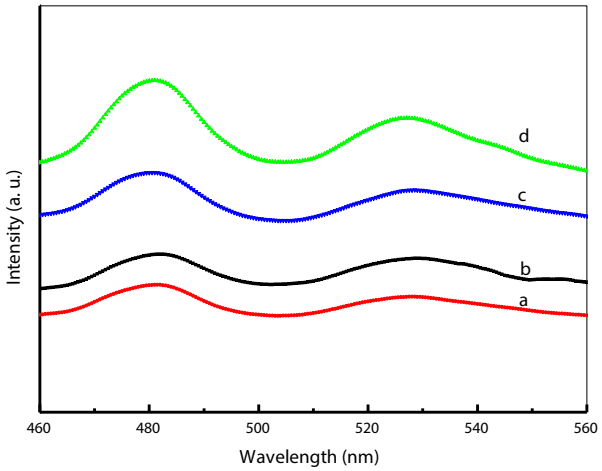

Fig. 7 – PL of (a) $(Cr_2O_3)_{0.20}$ $(NiO)_{0.80}$, (b) $(Cr_2O_3)_{0.40}$ $(NiO)_{0.60}$, (c) $(Cr_2O_3)_{0.60}$ $(NiO)_{0.40}$, and (d) $(Cr_2O_3)_{0.80}$ $(NiO)_{0.20}$ nanoparticles at calcination temperature of 700 °C.

reduction of the bandgap. Thus, when the energy regime is higher, the conduction bands of the s-electrons and p-electrons become severed. Hence, the overlap may occur in conditions with small-sized particles. Regarding the Fermi level distance, which is far away from the particle's center, the nuclear potential for electrons conduction is low. Consequently, transitions with allowed quantum numbers will be associated with an absorption energy that amounts to the conduction band energy. To facilitate comparative analysis, band gap values were lowered while the x values were increased (see Table 2). When x increases, this may grow the defected states, thus incrementing the absorption coefficient. Photon absorption produces electron–hole pairs, which can change the features of the optical nanomaterial and its electronic structure.

3.7. *PL analysis*

To study the photoluminescence possessions of the produced $(Cr_2O_3)_x$ $(NiO)_{1-x}$ nanoparticles, the samples have been examined at excitation of 390 nm as shown in Fig. 7. Under excitation of 390 nm, the PL spectra for sample nanoparticles synthesized in poly (vinyl alcohol) and various precursor concentrations were recorded at room temperature. Fig. 7 shows that the PL spectra for the sample nanoparticles produced in poly (vinyl alcohol) had a broad emission, scattering over a range of approximately 465–550 nm. This can be attributed to the compounded effect, as well as the energy states associated with the valence and conduction bands. In the case of the broad peaks, they constitute a pair of sub bands at approximately 480 and 527 nm, which are not as distinctive. The initial such band is interpreted as the recombination of electron–hole pairs in vacancies of metal and oxygen [105,106]. As for the next peak (green-yellow emissions centred at 527 nm), this is clearly visible in the PL spectra of metal oxide nanoparticles, which are transitioning between valence and conduction bands. Notably, intensification of the PL intensities was observed to correlate with higher x values, and the maximum was attained at x = 0.80 mmol, which was also closely related to the maximum attained crystallinity. After comparatively examining a range of precursor concentrations where an increase in the x value generated an increase in intensity, it was found that the most intense peaks against the weak spectral bands produced x values lower than 0.80. This indicated that, for x's values, they are noteworthy in attaining a sample morphology marked by high surface and structural regularity.

4. Conclusion

This study's findings indicate that $(Cr_2O_3)_x$ $(NiO)_{1-x}$ nanoparticles can be prepared successfully using the calcination method. The $(Cr_2O_3)_x$ $(NiO)_{1-x}$ nanoparticles have been found in a face-centred cubic and hexagonal structures for nickel oxide and chromium oxide, respectively. This occurred at all x values, using X-Ray Diffraction investigation. The particles' size has been directly proportional to the x value, and the sizes ranged from 5 to 16 nm at x = 0.20–0.80. The FT-IR spectrum indicated the main vibrational modes of Cr–O and Ni–O. The energy bandgap decreased with a higher x value (as indicated using the UV–Vis absorption spectrum). In the case of the luminescence spectrum, photoluminescence intensity was directly and proportionally related to particle size. The obtained results have revealed that the smaller particle size is obtained from lower x values, and the smaller energy band gap is obtained from higher x values. From these results, it is suggested that the product at lower x values and higher x values can be used with antibacterial activity and solar cell energy applications, respectively.

Contributions

N.M.A conceived and designed the experiments; N.M.A, A.M.A and MAS performed the experiments; NMA, A.M.A, M.A.S and H.K analyzed the data; N.M.A, H.K, AHS, A.M.A and N.M.A, JW,

contributed reagents/materials/analysis tools; N.M.A, A.M.A and MAS wrote the paper. All authors reviewed the manuscript.

Declaration of Competing Interest

The authors declare that they have no known competing financial interests or personal relationships that could have appeared to influence the work reported in this paper.

Acknowledgment

This work was supported in part by the Research Foundation for Advanced Talents of Dezhou University, China, in part by the Universiti Tenaga Nasional (UNITEN), Malaysia, under Grant UNITEN/RMC(BOLD); Grant code: RJO10517844/007.

REFERENCES

[1] Yao J, Yang M, Duan Y. Chemistry, biology, and medicine of fluorescent nanomaterials and related systems: new insights into biosensing, bioimaging, genomics, diagnostics, and therapy. Chem Rev 2014;114(12):6130–78.
[2] Aziz N, Pandey R, Barman I, Prasad R. Leveraging the attributes of Mucor hiemalis-derived silver nanoparticles for a synergistic broad-spectrum antimicrobial platform. Front Microbiol 2016;7:1984.
[3] Marpu SB, Benton EN. Shining light on chitosan: a review on the usage of chitosan for photonics and nanomaterials research. Int J Mol Sci 2018;19(6):1795.
[4] Al-Hada NM, Al-Ghaili AM, Kasim H, Saleh MA, Flaifel MH, Kamari HM, et al. The effect of PVP concentration on particle size, morphological and optical properties of cassiterite nanoparticles. IEEE Access 2020;8:93444–54.
[5] Muhamad S, Kamari HM, Al-Hada NM, Abdullah CAC, Nidzam NNS. Fabrication of binary (ZnO) x (TiO 2) 1– x nanoparticles via thermal treatment route and evaluating the impact of various molar concentrations on the structure and optical behaviors. Appl Phys A 2020;126(8):1–15.
[6] Kibasomba PM, Dhlamini S, Maaza M, Liu CP, Rashad MM, Rayan DA, et al. Strain and grain size of TiO2 nanoparticles from TEM, Raman spectroscopy and XRD: the revisiting of the Williamson-Hall plot method. Results Physics 2018;9:628–35.
[7] Anari-Anaraki M, Nezamzadeh-Ejhieh A. Modification of an Iranian clinoptilolite nano-particles by hexadecyltrimethyl ammonium cationic surfactant and dithizone for removal of Pb (II) from aqueous solution. J Colloid Interface Sci 2015;440:272–81.
[8] Sheikh-Mohseni MH, Nezamzadeh-Ejhieh A. Modification of carbon paste electrode with Ni-clinoptilolite nanoparticles for electrocatalytic oxidation of methanol. Electrochim Acta 2014;147:572–81.
[9] Zakiyah LB, Saion E, Al-Hada NM, Gharibshahi E, Salem A, Soltani N, et al. Up-scalable synthesis of size-controlled copper ferrite nanocrystals by thermal treatment method. Mater Sci Semicond Process 2015;40:564–9.
[10] Khan I, Saeed K, Khan I. Nanoparticles: properties, applications and toxicities. Arabian J Chem 2019;12(7):908–31.
[11] Han Y-H, Kankala RK, Wang S-B, Chen A-Z. Leveraging engineering of indocyanine green-encapsulated polymeric nanocomposites for biomedical applications. Nanomaterials 2018;8(6):360.
[12] Veiseh O, Gunn JW, Zhang M. Design and fabrication of magnetic nanoparticles for targeted drug delivery and imaging. Adv Drug Deliv Rev 2010;62(3):284–304.
[13] Kumar KS, Choudhary N, Jung Y, Thomas J. Recent advances in two-dimensional nanomaterials for supercapacitor electrode applications. ACS Energy Letters 2018;3(2):482–95.
[14] Jafari S, Nezamzadeh-Ejhieh A. Supporting of coupled silver halides onto clinoptilolite nanoparticles as simple method for increasing their photocatalytic activity in heterogeneous photodegradation of mixture of 4-methoxy aniline and 4-chloro-3-nitro aniline. J Colloid Interface Sci 2017;490:478–87.
[15] Derikvandi H, Nezamzadeh-Ejhieh A. Designing of experiments for evaluating the interactions of influencing factors on the photocatalytic activity of NiS and SnS2: focus on coupling, supporting and nanoparticles. J Colloid Interface Sci 2017;490:628–41.
[16] Alswata AA, Ahmad MB, Al-Hada NM, Kamari HM, Hussein MZB, Ibrahim NA. Preparation of zeolite/zinc oxide nanocomposites for toxic metals removal from water. Results Physics 2017;7:723–31.
[17] Al-Hada NM, Kamari HM, Baqer AA, Shaari AH, Saion E. Thermal calcination-based production of SnO2 nanopowder: an analysis of SnO2 nanoparticle characteristics and antibacterial activities. Nanomaterials 2018;8(4):250.
[18] Baqer AA, Matori KA, Al-Hada NM, Kamari HM, Shaari AH, Saion E, et al. Copper oxide nanoparticles synthesized by a heat treatment approach with structural, morphological and optical characteristics. J Mater Sci Mater Electron 2018;29(2):1025–33.
[19] Gene SA, Saion E, Shaari AH, Kamarudin MA, Al-Hada NM, Kharazmi A. Structural, optical, and magnetic characterization of spinel zinc chromite nanocrystallines synthesised by thermal treatment method. J Nanomater 2014:2014.
[20] Salem A, Saion E, Al-Hada NM, Kamari HM, Shaari AH, Radiman S. Simple synthesis of ZnSe nanoparticles by thermal treatment and their characterization. Results Physics 2017;7:1175–80. https://doi.org/10.1016/j.rinp.2017.03.011.
[21] Ahmed N, Fessi H, Elaissari A. Theranostic applications of nanoparticles in cancer. Drug Discov Today 2012;17(17–18):928–34.
[22] Kabashin AV, Singh A, Swihart MT, Zavestovskaya IN, Prasad PN. Laser-processed nanosilicon: a multifunctional nanomaterial for energy and healthcare. ACS Nano 2019;13(9):9841–67.
[23] Khalil AT, Ovais M, Ollah I, Ali M, Shinwari ZK, Khamlich S, et al. Sageretia thea (Osbeck.) mediated synthesis of zinc oxide nanoparticles and its biological applications. Nanomedicine 2017;12(15):1767–89.
[24] Khalil AT, Ovais M, Ullah I, Ali M, Shinwari ZK, Maaza M. Physical properties, biological applications and biocompatibility studies on biosynthesized single phase cobalt oxide (Co3O4) nanoparticles via Sageretia thea (Osbeck.). Arabian J Chem 2020;13(1):606–19.
[25] Nezamzadeh-Ejhieh A, Tavakoli-Ghinani S. Effect of a nano-sized natural clinoptilolite modified by the hexadecyltrimethyl ammonium surfactant on cephalexin drug delivery. Compt Rendus Chem 2014;17(1):49–61.
[26] Derikvandi H, Nezamzadeh-Ejhieh A. Comprehensive study on enhanced photocatalytic activity of heterojunction ZnS-

NiS/zeolite nanoparticles: experimental design based on response surface methodology (RSM), impedance spectroscopy and GC-MASS studies. J Colloid Interface Sci 2017;490:652–64.
[27] Borandegi M, Nezamzadeh-Ejhieh A. Enhanced removal efficiency of clinoptilolite nano-particles toward Co (II) from aqueous solution by modification with glutamic acid. Colloid Surface Physicochem Eng Aspect 2015;479:35–45.
[28] Al-Hada NM, Saion E, Kamari HM, Falifel MH, Shaari AH, Talib ZA, et al. Structural, morphological and optical behaviour of PVP capped binary (ZnO) 0.4 (CdO) 0.6 nanoparticles synthesised by a facile thermal route. Mater Sci Semicond Process 2016;53:56–65.
[29] Hashem M, Saion E, Al-Hada NM, Kamari HM, Shaari AH, Talib ZA, et al. Fabrication and characterization of semiconductor nickel oxide (NiO) nanoparticles manufactured using a facile thermal treatment. Results Physics 2016;6:1024–30.
[30] Salem A, Saion E, Al-Hada NM, Kamari HM, Shaari AH, Abdullah CAC, et al. Synthesis and characterization of CdSe nanoparticles via thermal treatment technique. Results in physics 2017;7:1556–62.
[31] Navarrete E, Bittencourt C, Umek P, Llobet E. AACVD and gas sensing properties of nickel oxide nanoparticle decorated tungsten oxide nanowires. J Mater Chem C 2018;6(19):5181–92.
[32] Iqbal J, Abbasi BA, Ahmad R, Mahmoodi M, Munir A, Zahra SA, et al. Phytogenic synthesis of nickel oxide nanoparticles (NiO) using fresh leaves extract of rhamnus triquetra (wall.) and investigation of its multiple in vitro biological potentials. Biomedicines 2020;8(5):117.
[33] Singh J, Kumar R, Verma V, Kumar R. Role of Ni2+ substituent on the structural, optical and magnetic properties of chromium oxide (Cr2-xNixO3) nanoparticles. Ceram Int 2020;46(15):24071–82.
[34] Peymanfar R, Khodamoradipoor N. Preparation and characterization of copper chromium oxide nanoparticles using modified sol-gel route and evaluation of their microwave absorption properties. Phys Status Solidi 2019;216(11):1900057.
[35] Ahmadi A, Nezamzadeh-Ejhieh A. A comprehensive study on electrocatalytic current of urea oxidation by modified carbon paste electrode with Ni (II)-clinoptilolite nanoparticles: experimental design by response surface methodology. J Electroanal Chem 2017;801:328–37.
[36] Madelung O. Semiconductors: group IV elements and III-V compounds. Springer Science & Business Media; 2012.
[37] Sharma N, Ojha H, Bharadwaj A, Pathak DP, Sharma RK. Preparation and catalytic applications of nanomaterials: a review. RSC Adv 2015;5(66):53381–403.
[38] Arabpour N, Nezamzadeh-Ejhieh A. Photodegradation of cotrimaxazole by clinoptilolite-supported nickel oxide. Process Saf Environ Protect 2016;102:431–40.
[39] Senobari S, Nezamzadeh-Ejhieh A. A pn junction NiO-CdS nanoparticles with enhanced photocatalytic activity: a response surface methodology study. J Mol Liq 2018;257:173–83.
[40] Al-Hada NM, Kamari HM, Saleh MA, Flaifel MH, Al-Ghaili AM, Kasim H, et al. Morphological, structural and optical behaviour of PVA capped binary (NiO)0.5 (Cr2O3)0.5 nanoparticles produced via single step based thermal technique. Results in Physics 2020;17:103059. https://doi.org/10.1016/j.rinp.2020.103059.
[41] Yahya N. Green urea: for future sustainability. Springer; 2018.
[42] Ahmed AA, Hashim M, Abdalrheem R, Rashid M. High-performance multicolor metal-semiconductor-metal Si photodetector enhanced by nanostructured NiO thin film. J Alloys Compd 2019;798:300–10.
[43] Liu L, Liu Y, Li L, Wu Y, Singh M, Zhu B. The composite electrolyte with an insulation Sm2O3 and semiconductor NiO for advanced fuel cells. Int J Hydrogen Energy 2018;43(28):12739–47.
[44] Diallo A, Kaviyarasu K, Ndiaye S, Mothudi BM, Ishaq A, Rajendran V, et al. Structural, optical and photocatalytic applications of biosynthesized NiO nanocrystals. Green Chem Lett Rev 2018;11(2):166–75.
[45] D'Amario L, Jiang R, Cappel UB, Gibson EA, Boschloo G, Rensmo H, et al. Chemical and physical reduction of high valence Ni states in mesoporous NiO film for solar cell application. ACS Appl Mater Interfaces 2017;9(39):33470–7.
[46] Etefa HF, Imae T, Yanagida M. Enhanced photosensitization by carbon dots Co-adsorbing with dye on p-type semiconductor (nickel oxide) solar cells. ACS Appl Mater Interfaces 2020;12(16):18596–608.
[47] Majhi SM, Naik GK, Lee HJ, Song HG, Lee CR, Lee IH, et al. Au@ NiO core-shell nanoparticles as a p-type gas sensor: novel synthesis, characterization, and their gas sensing properties with sensing mechanism. Sensor Actuator B Chem 2018;268:223–31.
[48] Paulose R, Mohan R, Parihar V. Nanostructured nickel oxide and its electrochemical behaviour—a brief review. Nano-Structures & Nano-Objects 2017;11:102–11.
[49] Ezhilarasi AA, Vijaya JJ, Kaviyarasu K, Maaza M, Ayeshamariam A, Kennedy LJ. Green synthesis of NiO nanoparticles using Moringa oleifera extract and their biomedical applications: cytotoxicity effect of nanoparticles against HT-29 cancer cells. J Photochem Photobiol B Biol 2016;164:352–60.
[50] Rani BJ, Ravi G, Yuvakkumar R, Ravichandran S, Ameen F, Al-Sabri A. Efficient, highly stable Zn-doped NiO nanocluster electrocatalysts for electrochemical water splitting applications. J Sol Gel Sci Technol 2019;89(2):500–10.
[51] Ting YH, Chen JY, Huang CW, Huang TK, Hsieh CY, Wu WW. Observation of resistive switching behavior in crossbar core–shell Ni/NiO nanowires memristor. Small 2018;14(6):1703153.
[52] Zhang K, Ye X, Shen Y, Cen Z, Xu K, Yang F. Interface engineering of Co 3 O 4 nanowire arrays with ultrafine NiO nanowires for high-performance rechargeable alkaline batteries. Dalton Trans 2020;49(25):8582–90.
[53] Su C, Zhang L, Han Y, Ren C, Zeng M, Zhou Z, et al. Controllable synthesis of heterostructured CuO–NiO nanotubes and their synergistic effect for glycol gas sensing. Sensor Actuator B Chem 2020;304:127347.
[54] Kumar YA, Kumar KD, Kim H-J. Facile preparation of a highly efficient NiZn 2 O 4–NiO nanoflower composite grown on Ni foam as an advanced battery-type electrode material for high-performance electrochemical supercapacitors. Dalton Trans 2020;49(11):3622–9.
[55] Qin Y, Wang Y, Yu C, Cui J, Yu D, Wu Y. Construction of high sensitivity non-enzymatic glucose sensor based on three-dimensiona nickel foam supported Ni2P/NiO/CeO2 nanoflake arrays. In: IOP Conference series: materials science and engineering, vol. 733. IOP Publishing; 2020. 012019.
[56] Jeong SY, Moon YK, Kim TH, Park SW, Kim KB, Kang YC, et al. A new strategy for detecting plant hormone ethylene using oxide semiconductor chemiresistors: exceptional gas selectivity and response tailored by nanoscale Cr2O3 catalytic overlayer. Advanced Science 2020;7(7):1903093.
[57] Ahmed Mohamed HE, Afridi S, Khalil AT, Zohra T, Ali M, Alam MM, et al. Phyto-fabricated Cr2O3 nanoparticle for

multifunctional biomedical applications. Nanomedicine 2020;15(17). https://doi.org/10.2217/nnm-2020-0129.
[58] Santhi N, Subashri K, Prabhakaran B. Hierarchically structure CrO 4–TiO 2 nanocomposite material and its multi application. J Mater Sci Mater Electron 2018;29(17):15074–85.
[59] Vafaei M, Mohammadi M. Impact of chromium doping on physical, optical, electronic and photovoltaic properties of nanoparticle TiO 2 photoanodes in dye-sensitized solar cells. New J Chem 2017;41(23):14516–27.
[60] Al Nafiey A, Addad A, Sieber B, Chastanet G, Barras A, Szunerits S, et al. Reduced graphene oxide decorated with Co3O4 nanoparticles (rGO-Co3O4) nanocomposite: a reusable catalyst for highly efficient reduction of 4-nitrophenol, and Cr (VI) and dye removal from aqueous solutions. Chem Eng J 2017;322:375–84.
[61] Huang WT, Cheng CL, Bao Z, Yang CW, Lu KM, Kang CY, et al. Broadband Cr3+, Sn4+-doped oxide nanophosphors for infrared mini light-emitting diodes. Angew Chem Int Ed 2019;58(7):2069–72.
[62] Choi S, Bonyani M, Sun G-J, Lee JK, Hyun SK, Lee C. Cr2O3 nanoparticle-functionalized WO3 nanorods for ethanol gas sensors. Appl Surf Sci 2018;432:241–9.
[63] Yadav AN, Singh K. Antiferromagnetic exchange in ultrasmall, uniform, and monodisperse chromium oxide nanocrystals. Mater Lett 2019;252:84–7.
[64] Fronzi M, Nolan M. Surface modification of perfect and hydroxylated TiO2 rutile (110) and anatase (101) with chromium oxide nanoclusters. ACS Omega 2017;2(10):6795–808.
[65] Woodard M, Akin S, Dibble C, Duncan M. Laser synthesis and spectroscopy of ligand-coated chromium oxide nanoclusters. J Phys Chem 2018;122(14):3606–20.
[66] Ashraf MA, Liu Z, Zheng D, Li C, Peng W-X, Fakhri A. Photocatalytic performance of novel chromium oxide-silicon dioxide decorated on multi-walled carbon nanotubes and graphene oxide nanocomposites: preparation, structural, and optimization. Phys E Low-dimens Syst Nanostruct 2020;116:113723.
[67] Kohli N, Singh RC. Comparative study of chromium oxide nanorods and nanoparticles as ethanol sensors. In: 2016 3rd international conference on emerging electronics (ICEE). IEEE; 2016. p. 1–3.
[68] Phu ND, Sy TX, Cao HT, Dinh NN, Thien LV, Hieu NM, et al. Amorphous iron-chromium oxide nanoparticles prepared by sonochemistry. J Non-Cryst Solids 2012;358(3):537–43.
[69] Anandan K, Rajendran V. Studies on structural, morphological, magnetic and optical properties of chromium sesquioxide (Cr2O3) nanoparticles: synthesized via facile solvothermal process by different solvents. Mater Sci Semicond Process 2014;19:136–44.
[70] Singh J, Verma V, Kumar R. Preparation and structural, optical studies of Al substituted chromium oxide (Cr2O3) nanoparticles. Vacuum 2019;159:282–6.
[71] Deepak HN, Choudhari K, Shivashankar S, Santhosh C, Kulkarni SD. Facile microwave-assisted synthesis of Cr2O3 nanoparticles with high near-infrared reflection for roof-top cooling applications. J Alloys Compd 2019;785:747–53.
[72] Kamari HM, Al-Hada NM, Baqer AA, Shaari AH, Saion E. Comprehensive study on morphological, structural and optical properties of Cr 2 O 3 nanoparticle and its antibacterial activities. J Mater Sci Mater Electron 2019;30(8):8035–46.
[73] Mohammad E, Kareem M, Atiyah A. Synthesis of carbon nanotubes from graphite and investigation of the catalytic activity of MWCNTs/Cr2O3–NiO with the removal of bismarck Brown G dye from its aqueous solution. Ukrainian J Phys 2019;64(4). 276-276.
[74] Chusuei CC, Wu CH, Mallavarapu S, Hou FYS, Hsu CM, Aronstam RS, et al. Physicochemical structure effects on metal oxide nanoparticulate cytotoxicity. In: Recent progress in colloid and surface chemistry with biological applications. ACS Publications; 2015. p. 137–55.
[75] Zoromba MS, Bassyouni M, Aziz MHA, Al-Hossainy AF, Salah N, Al-Ghamdi AA, et al. Structure and photoluminescence characteristics of mixed nickel–chromium oxides nanostructures. Appl Phys A 2019;125(9):642.
[76] Tilley RD, Jefferson DA. The preparation of chromium, nickel and chromium–nickel alloy nanoparticles on supports. J Mater Chem 2002;12(12):3809–13.
[77] Al-Hada NM, Kamari HM, Abdullah CAC, Saion E, Shaari AH, Talib ZA, et al. Down-top nanofabrication of binary (CdO) x (ZnO) 1–x nanoparticles and their antibacterial activity. Int J Nanomed 2017;12:8309.
[78] Villa A, Wang D, Su DS, Prati L. Gold sols as catalysts for glycerol oxidation: the role of stabilizer. ChemCatChem 2009;1(4):510–4.
[79] Luo Y, Sun X. One-step preparation of poly (vinyl alcohol)-protected Pt nanoparticles through a heat-treatment method. Mater Lett 2007;61(10):2015–7.
[80] Bogle K, Dhole S, Bhoraskar V. Silver nanoparticles: synthesis and size control by electron irradiation. Nanotechnology 2006;17(13):3204.
[81] Al-Hada NM, Saion E, Talib ZA, Shaari AH. The impact of polyvinylpyrrolidone on properties of cadmium oxide semiconductor nanoparticles manufactured by heat treatment technique. Polymers 2016;8(4):113.
[82] Al-Hada NM, Saion EB, Shaari AH, Kamarudeen MA, Flaifel MH, Gene SA. Synthesis, structural and morphological properties of cadmium oxide nanoparticles prepared by thermal treatment method. In: Advanced materials research, vol. 1107. Trans Tech Publ; 2015. p. 291–4.
[83] Baqer AA, Matori KA, Al-Hada NM, Shaari AH, Kamari HM, Saion E, et al. Synthesis and characterization of binary (CuO) 0.6 (CeO2) 0.4 nanoparticles via a simple heat treatment method. Results Physics 2018;9:471–8.
[84] Gene SA, Saion EB, Shaari AH, Kamarudeen MA, Al-Hada NM. Fabrication and characterization of nanospinel ZnCr2O4 using thermal treatement method. In: Advanced materials research, vol. 1107. Trans Tech Publ; 2015. p. 301–7.
[85] Midala IH, Kamari HM, Al-Hada NM, Tim CK, Muhamad S, Hamza AM, et al. Structural, morphological and optical properties of (ZnO) 0.2 (ZrO 2) 0.8 nanoparticles. Appl Phys A 2019;125(9):668.
[86] Amani-Beni Z, Nezamzadeh-Ejhieh A. NiO nanoparticles modified carbon paste electrode as a novel sulfasalazine sensor. Anal Chim Acta 2018;1031:47–59.
[87] Senobari S, Nezamzadeh-Ejhieh A. A comprehensive study on the enhanced photocatalytic activity of CuO-NiO nanoparticles: designing the experiments. J Mol Liq 2018;261:208–17.
[88] Zak AK, Majid WA, Abrishami ME, Yousefi R. X-ray analysis of ZnO nanoparticles by Williamson–Hall and size–strain plot methods. Solid State Sci 2011;13(1):251–6.
[89] Al-Hada NM, Saion E, Shaari AH, Kamarudin MA, Flaifel MH, Ahmad SH, et al. A facile thermal-treatment route to synthesize ZnO nanosheets and effect of calcination temperature. PloS One 2014;9(8):e103134.
[90] Baqer AA, Matori KA, Al-Hada NM, Shaari AH, Saion E, Chyi JLY. Effect of polyvinylpyrrolidone on cerium oxide nanoparticle characteristics prepared by a facile heat treatment technique. Results in physics 2017;7:611–9.
[91] Al-Hada NM, Kamari HM, Shaari AH, Saion E. Fabrication and characterization of Manganese–Zinc Ferrite

nanoparticles produced utilizing heat treatment technique. Results in Physics 2019;12:1821–5. https://doi.org/10.1016/j.rinp.2019.02.019.
[92] Al-Hada NM, Saion EB, Shaari AH, Kamarudin MA, Flaifel MH, Ahmad SH, et al. A facile thermal-treatment route to synthesize the semiconductor CdO nanoparticles and effect of calcination. Mater Sci Semicond Process 2014;26:460–6. https://doi.org/10.1016/j.mssp.2014.05.032.
[93] Kamari HM, Al-Hada NM, Saion E, Shaari AH, Talib ZA, Flaifel MH, et al. Calcined solution-based PVP influence on ZnO semiconductor nanoparticle properties. Crystals 2017;7(2):2.
[94] Lee PJ, Saion E, Al-Hada NM, Soltani N. A simple up-scalable thermal treatment method for synthesis of ZnO nanoparticles. Metals 2015;5(4):2383–92.
[95] Nezamzadeh-Ejhieh A, Shahanshahi M. Modification of clinoptilolite nano-particles with hexadecylpyridynium bromide surfactant as an active component of Cr (VI) selective electrode. J Ind Eng Chem 2013;19(6):2026–33.
[96] Derikvandi H, Nezamzadeh-Ejhieh A. Synergistic effect of pn heterojunction, supporting and zeolite nanoparticles in enhanced photocatalytic activity of NiO and SnO2. J Colloid Interface Sci 2017;490:314–27.
[97] Wang D, Niu F, Mortelliti MJ, Sheridan MV, Sherman BD, Zhu Y, et al. A stable dye-sensitized photoelectrosynthesis cell mediated by a NiO overlayer for water oxidation. Proc Natl Acad Sci Unit States Am 2020;117(23):12564–71.
[98] Derikvandi H, Nezamzadeh-Ejhieh A. Increased photocatalytic activity of NiO and ZnO in photodegradation of a model drug aqueous solution: effect of coupling, supporting, particles size and calcination temperature. J Hazard Mater 2017;321:629–38.
[99] Babaahamdi-Milani M, Nezamzadeh-Ejhieh A. A comprehensive study on photocatalytic activity of supported Ni/Pb sulfide and oxide systems onto natural zeolite nanoparticles. J Hazard Mater 2016;318:291–301.
[100] Khodami Z, Nezamzadeh-Ejhieh A. Investigation of photocatalytic effect of ZnO–SnO2/nano clinoptilolite system in the photodegradation of aqueous mixture of 4-methylbenzoic acid/2-chloro-5-nitrobenzoic acid. J Mol Catal Chem 2015;409:59–68.
[101] Rezaei M, Nezamzadeh-Ejhieha A. The ZnO-NiO nano-composite: a brief characterization, kinetic and thermodynamic study and study the Arrhenius model on the sulfasalazine photodegradation. Int J Hydrogen Energy 2020;45(46):24749–64.
[102] Khamlich S, Nuru ZY, Bello A, Fabiane M, Dangbegnon JK, Manyala N, et al. Pulsed laser deposited Cr2O3 nanostructured thin film on graphene as anode material for lithium-ion batteries. J Alloys Compd 2015;637:219–25.
[103] Khamlich S, Nemraoui O, Mongwaketsi N, McCrindle R, Cingo N, Maaza M. Black Cr/α-Cr2O3 nanoparticles based solar absorbers. Phys B Condens Matter 2012;407(10):1509–12.
[104] Khamlich S, McCrindle R, Nuru Z, Cingo N, Maaza M. Annealing effect on the structural and optical properties of Cr/α-Cr2O3 monodispersed particles based solar absorbers. Appl Surf Sci 2013;265:745–9.
[105] Thema F, Manikandan E, Gurib-Fakim A, Maaza M. Single phase Bunsenite NiO nanoparticles green synthesis by Agathosma betulina natural extract. J Alloys Compd 2016;657:655–61.
[106] Khalil AT, Ovais M, Ullah I, Ali M, Shinwari ZK, Hassan D, et al. Sageretia thea (Osbeck.) modulated biosynthesis of NiO nanoparticles and their in vitro pharmacognostic, antioxidant and cytotoxic potential. Artificial cells, Nanomed Biotechnology 2018;46(4):838–52.